

# Breathing pyrochlore magnet $\text{CuGaCr}_4\text{S}_8$ : Magnetic, thermodynamic, and dielectric properties

Masaki Gen,<sup>1,2,\*</sup> Hajime Ishikawa,<sup>3</sup> Atsushi Miyake,<sup>3</sup> Takeshi Yajima,<sup>3</sup> Harald O. Jeschke,<sup>4</sup>  
Hajime Sagayama,<sup>5</sup> Akihiko Ikeda,<sup>3,6</sup> Yasuhiro H. Matsuda,<sup>3</sup> Koichi Kindo,<sup>3</sup> Masashi Tokunaga,<sup>3</sup>  
Yoshimitsu Kohama,<sup>3</sup> Takashi Kurumaji,<sup>1</sup> Yusuke Tokunaga,<sup>1</sup> and Taka-hisa Arima<sup>1,2</sup>

<sup>1</sup>Department of Advanced Materials Science, The University of Tokyo, Kashiwa 277-8561, Japan

<sup>2</sup>RIKEN Center for Emergent Matter Science (CEMS), Wako 351-0198, Japan

<sup>3</sup>Institute for Solid State Physics, The University of Tokyo, Kashiwa 277-8581, Japan

<sup>4</sup>Research Institute for Interdisciplinary Science, Okayama University, Okayama 700-8530, Japan

<sup>5</sup>Institute of Materials Structure Science, High Energy Accelerator Research Organization, Tsukuba 305-0801, Japan

<sup>6</sup>Department of Engineering Science, University of Electro-Communications, Chofu, Tokyo 182-8585, Japan

(Dated: October 18, 2023)

We investigate the crystallographic and magnetic properties of a chromium-based thiospinel  $\text{CuGaCr}_4\text{S}_8$ . From a synchrotron x-ray diffraction experiment and structural refinement, Cu and Ga atoms are found to occupy the tetrahedral A-sites in an alternate way, yielding breathing pyrochlore Cr network.  $\text{CuGaCr}_4\text{S}_8$  undergoes a magnetic transition associated with a structural distortion at 31 K in zero magnetic field, indicating that the spin-lattice coupling is responsible for relieving the geometrical frustration. When applying a pulsed high magnetic field, a sharp metamagnetic transition takes place at 40 T, followed by a 1/2-magnetization plateau up to 103 T. These phase transitions accompany dielectric anomalies, suggesting the presence of helical spin correlations in low-field phases. The density-functional-theory calculations suggest that  $\text{CuGaCr}_4\text{S}_8$  is dominated by antiferromagnetic and ferromagnetic exchange couplings within small and large tetrahedra, respectively, in analogy with  $\text{CuInCr}_4\text{S}_8$ . We argue that A-site-ordered Cr thiospinels serve as an excellent platform to explore diverse magnetic phases along with pronounced magnetoelastic and magnetodielectric responses.

## I. INTRODUCTION

Magnetic materials of the pyrochlore lattice, a three-dimensional network of corner-sharing tetrahedra, have been a central research subject in the context of frustrated magnetism [1, 2]. In recent years, the *breathing* pyrochlore lattice, where up- and down-pointing tetrahedra differ in size, has attracted growing interest from the viewpoint of ground state control [3]. The key concept of this spin model lies in the introduction of inequivalent exchange couplings  $J$  and  $J'$  in the small and large tetrahedra, respectively [Fig. 1(a)]. Depending on the signs and magnitudes of  $J$  and  $J'$  as well as the nature of spins, various exotic magnetic states and emergent phenomena have been theoretically predicted: e.g., unconventional spin-liquid states and excitations [4–9], spin-lattice-coupled superlattice long-range orders (LROs) [10, 11], and a magnetic hedgehog-lattice [12, 13].

A representative realization of the breathing pyrochlore system is a quantum Heisenberg antiferromagnet  $\text{Ba}_3\text{Yb}_2\text{Zn}_5\text{O}_{11}$ , whose magnetism is governed by  $\text{Yb}^{3+}$  ions with pseudospin-1/2 [14]. In this compound, the breathing ratio  $r'/r$ , where  $r$  ( $r'$ ) represents the nearest-neighbor (NN) bond length in small (large) tetrahedra, amounts to approximately 2, resulting in  $J \gg J' > 0$ , i.e., close to the decoupled tetrahedron limit [14]. The magnetization, specific heat, and inelastic neutron scattering suggested the singlet formation without any signs of a magnetic LRO at low temperatures [14, 15], though the development of intertetrahedral correlations is also pointed out [16, 17].

For the larger spin case, A-site-ordered chromium-based spinels  $\text{AA}'\text{Cr}_4\text{X}_8$ , where  $\text{Cr}^{3+}$  ions with spin-3/2 form a

breathing pyrochlore lattice, offer a fertile playground to address an effective spin Hamiltonian with various sets of  $J$  and  $J'$  [18]. Due to the difference in the ionic radius between  $\text{A}^+$  and  $\text{A}'^{3+}$  cations, their crystallographic ordering like the zinc-blende-type arrangement should modulate the chemical pressure and as a consequence induce the breathing bond-alternation in the Cr pyrochlore network [Fig. 1(b)]. This material design was first proposed by Joubert and Durif in 1966 [19]. They prepared two oxides,  $\text{LiGaCr}_4\text{O}_8$  and  $\text{LiInCr}_4\text{O}_8$ , and found the lack of an inversion center in their crystal structures, signaling the ordering of Li and Ga/In atoms. Subsequently, Pinch *et al.* synthesized Cr thiospinels  $\text{AA}'\text{Cr}_4\text{S}_8$  with various combinations of A and A' atoms:  $\text{A}=\text{Li, Cu, Ag}$ ;  $\text{A}'=\text{Al, Ga, In}$  [20]. Among them, the A-site ordering was confirmed for  $\text{LiGaCr}_4\text{S}_8$ ,  $\text{LiInCr}_4\text{S}_8$ ,  $\text{CuAlCr}_4\text{S}_8$ , and  $\text{CuInCr}_4\text{S}_8$ . Structural refinements and detailed physical property measurements on these compounds have been actively performed in the last decade [21–32], triggered by the renewed interest by Okamoto *et al.* in 2013 [3].

It is noteworthy that a peculiar combination of antiferromagnetic (AFM)  $J$  and ferromagnetic (FM)  $J'$  can be realized in  $\text{AA}'\text{Cr}_4\text{X}_8$  due to the competition between the AFM Cr–Cr direct exchange and FM Cr–X–Cr superexchange interactions [18]. Such a spin Hamiltonian can be effectively mapped on the spin-6 Heisenberg antiferromagnet on the face-centered-cubic (FCC) lattice if  $J'$  is strong. Indeed, a cluster excitation was observed in  $\text{CuInCr}_4\text{S}_8$  at low temperatures [30], indicating the development of FM correlations within each large tetrahedron. Another characteristic feature is the intrinsic strong spin-lattice coupling (SLC) arising from the sensitivity of the strength of  $J$  ( $J'$ ) against the NN Cr–Cr bond length, i.e., large  $|dJ/dr|$  ( $|dJ'/dr'|$ ). The SLC can act as a principal perturbation to lift the macroscopic degeneracy and bring about magnetostructural transitions at low temperatures

\* masaki.gen@riken.jp

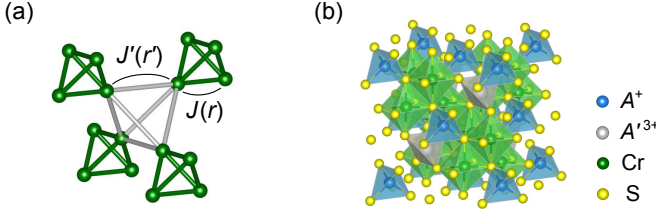


FIG. 1. (a) Schematic of a breathing pyrochlore lattice, where small and large tetrahedra with the nearest-neighbor bond lengths,  $r$  and  $r'$ , are characterized by the exchange interactions,  $J$  and  $J'$ , respectively. (b) Crystal structure of the A-site-ordered Cr spinels. The present focus is  $\text{CuGaCr}_4\text{S}_8$ , where nonmagnetic  $\text{Cu}^+$  and  $\text{Ga}^{3+}$  ions are found to be arranged in the zinc-blende-type structure, yielding a breathing pyrochlore Cr network. The illustrations are drawn with VESTA software [39].

[21–23, 28] and in an applied magnetic field [11, 26, 27]. Interestingly,  $\text{CuInCr}_4\text{S}_8$  exhibits a fascinating magnetic-field-versus-temperature ( $H$ - $T$ ) phase diagram including a robust 3-up-1-down phase associated with a  $1/2$ -magnetization plateau [27] as well as a thermal equilibrium phase pocket [32] reminiscent of a skyrmion lattice [33–35].

In this work, we report the structural, magnetic, thermodynamic, and dielectric properties of  $\text{CuGaCr}_4\text{S}_8$ . Although  $\text{CuGaCr}_4\text{S}_8$  was previously synthesized in Refs. [20, 36–38], no conclusive remark on the A-site ordering was given because the close proximity of the scattering factors between  $\text{Cu}^+$  and  $\text{Ga}^{3+}$  made it challenging to judge the presence or absence of reflections forbidden for the A-site disordered case, i.e.,  $(hk0)$  peaks with  $h + k = 4n + 2$ . Our synchrotron powder x-ray diffraction (XRD) measurement confirms the presence of 200 and 420 peaks of structural origin. The Rietveld analysis shows that the A-site-ordered spinel structure with the breathing pyrochlore Cr network ( $F\bar{4}3m$  space group) provides better refinement than the normal spinel structure ( $Fd\bar{3}m$  space group).  $\text{CuGaCr}_4\text{S}_8$  undergoes a magnetic transition at  $T_N = 31$  K in zero magnetic field. We observe a crystal symmetry lowering below  $T_N$ , which is compatible with the reported low-symmetry incommensurate helical structure and was overlooked in the previous neutron diffraction study [36]. A series of pulsed high-field experiments reveal that  $\text{CuGaCr}_4\text{S}_8$  exhibits a rich  $H$ - $T$  phase diagram associated with magnetoelastic and magnetodielectric effects, similar to that of  $\text{CuInCr}_4\text{S}_8$  [27, 32]. The effective spin Hamiltonian of  $\text{CuGaCr}_4\text{S}_8$  is discussed on the basis of the density-functional-theory (DFT) energy mapping as well as magnetoelastic theory [27].

## II. METHODS

Polycrystalline samples of  $\text{CuGaCr}_4\text{S}_8$  were synthesized by the conventional solid-state reaction method. Starting ingredients were high-purity gallium ingots (99.999%) and copper (99.99%), chromium (99.99%), and sulfur (99.99%) powders. They were mixed in the stoichiometric ratio, sealed in an evacuated quartz tube, and heated at 400°C for 24 h and then at

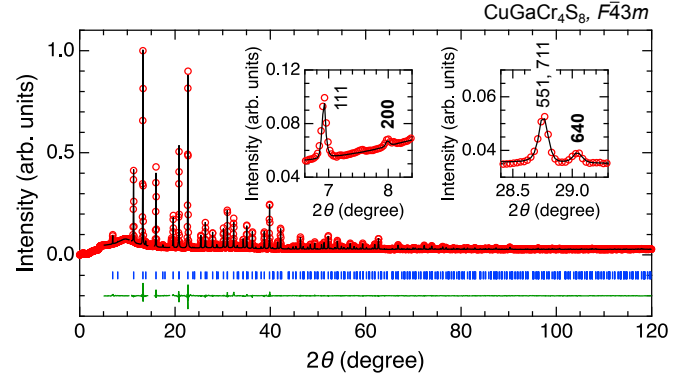


FIG. 2. Synchrotron XRD pattern of  $\text{CuGaCr}_4\text{S}_8$  powder samples (red open circle) and calculated XRD pattern obtained by the Rietveld analysis (black solid line). The Rietveld refinement was performed in a range of  $5^\circ < 2\theta < 120^\circ$ , where several tiny peaks originating from  $\text{Cr}_3\text{S}_4$  and unknown impurity phases are excluded. Blue vertical bars indicate the nuclear Bragg reflections, and the green line is the difference between the experimental and calculated patterns. Insets show enlarged views of the experimental XRD profiles focusing on 200 and 640 peaks, which are forbidden for  $Fd\bar{3}m$  but allowed for  $F\bar{4}3m$ .

800°C for 48 h in a box furnace. Then, the sintering was repeated twice at 900°C for 96 h after grinding and pelletizing the sintered products.

A powder synchrotron x-ray diffraction (XRD) profile was collected at room temperature on Photon Factory BL-8A. The wavelength was  $\lambda = 0.689739$  Å. The Rietveld analysis was performed using the RIETAN-FP program [40]. The temperature evolution of the powder XRD pattern was measured between 4 and 300 K using a commercial x-ray diffractometer (SmartLab, Rigaku) at the Institute for Solid State Physics (ISSP), University of Tokyo. The incident x-ray beam was monochromatized by a Johansson-type monochromator with a Ge(111) crystal to select only  $\text{Cu-K}\alpha 1$  radiation.

Magnetization up to 7 T was measured using a SQUID magnetometer (MPMS, Quantum Design). Magnetization up to 14 T was measured using a vibrating sample magnetometer installed in a physical property measurement system (PPMS, Quantum Design) equipped with a superconducting magnet. Magnetization up to 57 T was measured by the induction method in a non-destructive (ND) pulsed magnet ( $\sim 4$  ms duration). Magnetization up to 140 T was measured by the induction method using a coaxial-type pickup coil in a horizontal single-turn-coil (STC) megagauss generator ( $\sim 8$   $\mu\text{s}$  duration) [27]. Thermal expansion was measured by the fiber-Bragg-grating (FBG) method using an optical sensing instrument (Hyperion si155, LUNA) in a cryostat equipped with a superconducting magnet (Spectromag, Oxford) at zero field. Longitudinal magnetostriction up to 54 T was measured by the FBG method in a ND pulsed magnet ( $\sim 36$  ms duration), where the optical filter method was employed to detect the relative sample-length change  $\Delta L/L_0$  [41]. The fiber was attached to a rod-shaped sintered sample with epoxy Stycast1266. Dielectric constant at zero field was measured at a frequency of 10 kHz by using an LCR meter (E4980A, Agilent) in a PPMS.

TABLE I. Structural parameters of  $\text{CuGaCr}_4\text{S}_8$  at room temperature assuming the  $F\bar{4}3m$  space group, where Cu and Ga atoms occupy the  $4a$  and  $4d$  sites, respectively, and the atomic position  $x$  of Cr is less than 0.375. The lattice constant is  $a = 9.92036(8)$  Å. Reliability factors are  $R_{\text{wp}} = 2.826$ ,  $R_p = 1.755$ ,  $R_e = 1.711$ ,  $S = 1.6518$ .

		$x$	$y$	$z$	Occup.	B (Å)
Cu	$4a$	0	0	0	1	0.86(10)
Ga	$4d$	3/4	3/4	3/4	1	0.83(8)
Cr	$16e$	0.37042(15)	$x$	$x$	1	0.63(2)
S1	$16e$	0.13316(26)	$x$	$x$	1	0.79(5)
S2	$16e$	0.61679(21)	$x$	$x$	1	0.65(5)

Dielectric constant along the field direction ( $E \parallel B$ ) up to 48 T was measured at a frequency of 50 kHz by using a capacitance bridge (1615-A, General Radio) in a ND pulsed magnet ( $\sim 36$  ms duration) [42]. Silver paste was painted on the two large surfaces of a disk-shaped sintered sample to form electrodes. Heat capacity was measured by the thermal relaxation method in the PPMS at zero field. All the pulsed high-field experiments were performed at ISSP.

In our DFT energy mapping [43–45], we worked with the full potential local orbital basis set [46] and generalized gradient approximation (GGA) type exchange and correlation functional [47]. Strong electronic correlations on Cr  $3d$  orbitals were treated with DFT+ $U$  corrections [48], where we varied the onsite correlation strength  $U$  and fix the Hund’s rule coupling to  $J_H = 0.72$  eV [49]. We use a  $2 \times 2 \times 1$  supercell of  $\text{CuGaCr}_4\text{S}_8$  with  $Pm$  symmetry and twelve inequivalent  $\text{Cr}^{3+}$  positions to extract the exchange couplings up to the fifth NN.

### III. BASIC PHYSICAL PROPERTIES

#### A. Structural analysis

We first show that the crystal structure of  $\text{CuGaCr}_4\text{S}_8$  belongs to the  $F\bar{4}3m$  space group and consists of the breathing pyrochlore lattice, similar to the previously reported  $A$ -site-ordered Cr thiospinels [24, 31]. The synchrotron powder XRD pattern of  $\text{CuGaCr}_4\text{S}_8$  at room temperature is depicted by red open circles in Fig. 2. All major peaks can be indexed to the FCC symmetry characteristic of the spinel structure. We observe small additional peaks at  $2\theta = 7.98^\circ$  and  $29.04^\circ$  (insets of Fig. 2), indexed as the 200 and 640 reflections, respectively. Again,  $(hk0)$  peaks with  $h + k = 4n + 2$  are forbidden for  $Fd\bar{3}m$  but allowed for  $F\bar{4}3m$ . The possibility of impurity contribution to these peaks is excluded as long as we examine the known phases in the database (ICSD). The effect of multiple diffraction [50, 51] is minimal in our XRD measurement using the randomly oriented powder sample. The anisotropy of the local structure around the transition metal atoms could in principle break the forbidden rule of the  $Fd\bar{3}m$  space group without the  $A$ -site ordering [52], while the incident x-ray energy is sufficiently large compared to the resonance energies of the composition elements to suppress this factor.

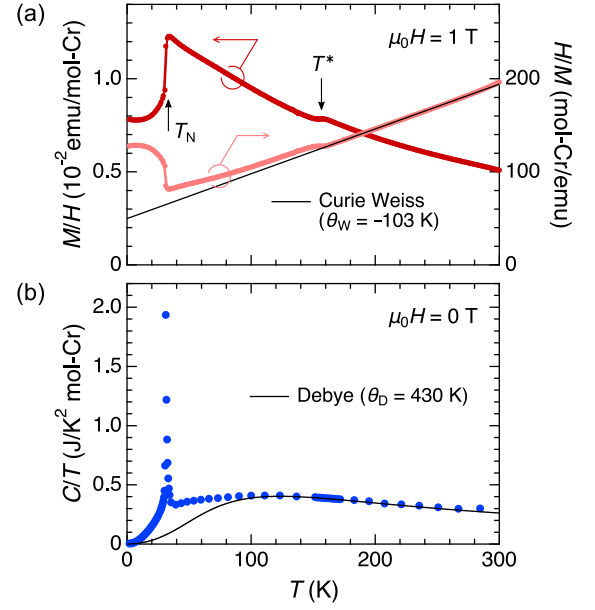


FIG. 3. Temperature dependence of (a) magnetic susceptibility  $M/H$  at 1 T and (b) heat capacity divided by temperature  $C/T$  at 0 T. The inverse magnetic susceptibility  $H/M$  and the Curie-Weiss fit above 160 K (black) are displayed in the right axis of (a). The solid line in (b) denotes the estimated lattice heat capacity based on the Debye model with the Debye temperature of  $\Theta_D = 430$  K.

Using the present XRD data, we performed the Rietveld analysis assuming several types of structural models. Details of the analysis are found in Appendix A. We confirm that the  $F\bar{4}3m$  model, assuming perfect  $A$ -site ordering and allowing the breathing distortion of the Cr pyrochlore lattice, yields better refinement than the  $Fd\bar{3}m$  model with random distribution of Cu and Ga atoms. The fitting result and structural parameters obtained for the  $F\bar{4}3m$  space group are shown in Fig. 2 and Table I, respectively. The lattice constant is  $a = 9.92036(8)$  Å, in accord with Ref. [20]. The NN Cr–Cr bond lengths are  $r = 3.377(4)$  Å and  $r' = 3.638(4)$  Å in small and large tetrahedra, respectively. The breathing ratio  $r'/r = 1.077$  is larger than those in oxides, 1.035 ( $\text{LiGaCr}_4\text{O}_8$ ) and 1.049 ( $\text{LiInCr}_4\text{O}_8$ ) [3], and comparable to those in other sulfides, 1.074 ( $\text{LiGaCr}_4\text{S}_8$ ), 1.089 ( $\text{LiInCr}_4\text{S}_8$ ) [24], 1.066 ( $\text{CuAlCr}_4\text{S}_8$ ) [31], and 1.084 ( $\text{CuInCr}_4\text{S}_8$ ) [32]. Although it is difficult to evaluate the ratio of site mixing between Cu and Ga, the refined value of  $r'/r$  is robust to the incorporation of the site mixing in the Rietveld analysis. We hence infer that Cu and Ga atoms are almost perfectly ordered in  $\text{CuGaCr}_4\text{S}_8$ , like in  $\text{Li}(\text{Ga}, \text{In})\text{Cr}_4\text{S}_8$  and  $\text{Cu}(\text{Al}, \text{In})\text{Cr}_4\text{S}_8$  [24, 31].

#### B. Magnetic and structural transitions at low temperatures

Figures 3(a) and 3(b) show the magnetic susceptibility  $M/H$  measured at 1 T and the heat capacity divided by temperature  $C/T$  measured at 0 T as a function of temperature, respectively. The inverse susceptibility  $H/M$  exhibits linear temperature dependence between 160 and 300 K [right



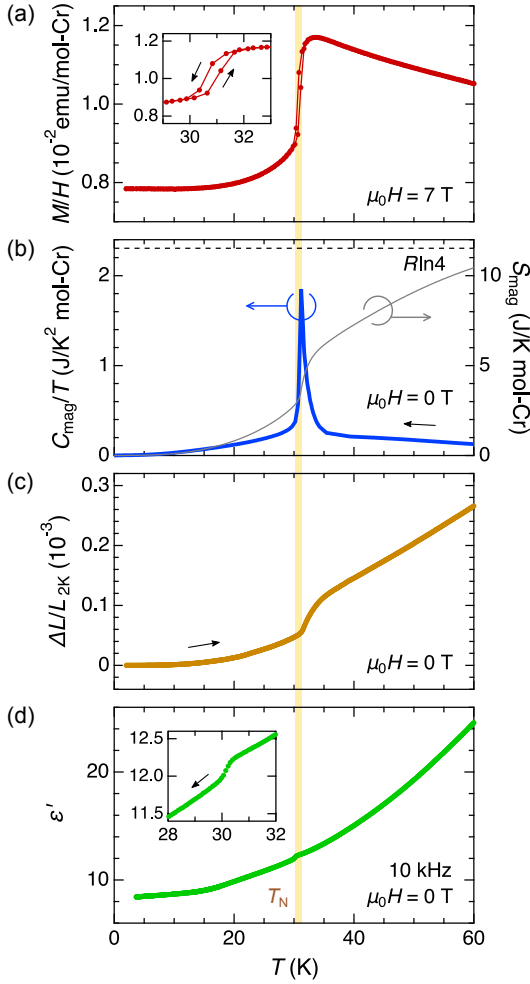


FIG. 4. Temperature dependence of (a) magnetic susceptibility  $M/H$  at 7 T, (b) magnetic heat capacity divided by temperature  $C_{\text{mag}}/T$  at 0 T, (c) thermal expansion  $\Delta L/L_{2K}$  at 0 T, and (d) dielectric constant  $\epsilon'$  at a frequency of 10 kHz at 0 T. The insets of (a) and (d) show enlarged views of  $M/H$  and  $\epsilon'$  around  $T_N$ , respectively. The magnetic entropy  $S_{\text{mag}}$  calculated by integrating  $C_{\text{mag}}/T$  with respect to temperature is displayed in the right axis of (b). Black arrows represent the direction of the temperature-sweeping process.

axis of Fig. 3(a)], following the Curie-Weiss law with the Weiss temperature of  $\Theta_W = -103$  K and the effective moment  $p_{\text{eff}} = 4.08 \mu_B$ . The large negative  $\Theta_W$  indicates dominant AFM exchange couplings, like  $\text{Cu}(\text{Al}, \text{In})\text{Cr}_4\text{S}_8$  [31, 32] but unlike  $\text{Li}(\text{Ga}, \text{In})\text{Cr}_4\text{S}_8$  [24, 25]. The estimated  $p_{\text{eff}}$  is slightly larger than the theoretical value of  $3.87 \mu_B$  expected for  $S = 3/2$  with quenched orbital moments, ensuring a nearly isotropic spin for  $\text{CuGaCr}_4\text{S}_8$ . In order to estimate lattice contributions to  $C/T$ , we employ the Debye model with the Debye temperature of  $\Theta_D = 430$  K as shown by a black line in Fig. 3(b). The calculated curve fits well to the experimental data above  $\sim 120$  K.

In the measured temperature range, we observe several anomalies in the  $M/H$ - $T$  curve [Fig. 3(a)].  $M/H$  exhibits a steplike anomaly at  $\sim 160$  K, below which  $H/M$  deviates from the linear temperature dependence. This could be attributed to

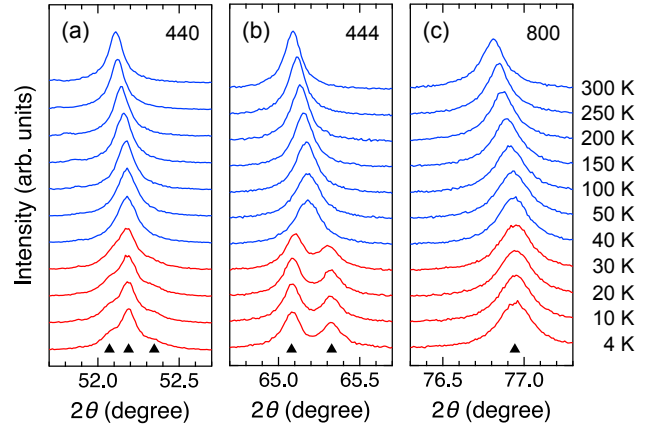


FIG. 5. Waterfall plots of the temperature evolution of the powder XRD pattern focusing on (a) 440, (b) 444, and (c) 800 reflections indexed for the cubic  $F\bar{4}3m$  space group. The data were obtained using a laboratory x-ray diffractometer with monochromatized  $\text{Cu-K}\alpha 1$  radiation. Triangles denote the peak positions obtained by the (multi-) Lorentzian fit to each peak profile.

the onset of short-range AFM correlations in the main phase or to an AFM transition in an unidentified impurity phase, which we will leave open for future interpretation. The inverse susceptibility  $H/M$  further exhibits a concave behavior below  $\sim 120$  K, where  $C/T$  deviates from the estimated lattice heat capacity [Fig. 3(b)], indicating the development of a magnetic short-range order. The similar feature was also observed for  $\text{CuInCr}_4\text{S}_8$  [24, 32]. On further cooling, an abrupt  $M/H$  drop and a sharp  $C/T$  peak are observed at  $T_N = 31$  K, indicating the onset of a magnetic LRO. The transition temperature is consistent with the previously reported values [20, 37, 38].

Figure 4 summarizes the temperature dependence of various physical quantities in the vicinity of  $T_N$ . As shown in the inset of Fig. 4(a),  $M/H$  shows a clear hysteresis, indicating that the magnetic transition is first order. Figure 4(b) shows the magnetic heat capacity divided by temperature  $C_{\text{mag}}/T$ , which is obtained by subtracting the estimated lattice contributions from the experimental  $C/T$  as shown in Fig. 3(b). By integrating  $C_{\text{mag}}/T$  with respect to temperature, the magnetic entropy  $S_{\text{mag}}$  is found to reach  $\sim 5$  J/(K mol-Cr) just above  $T_N$  [53]. We obtain  $S_{\text{mag}}$  at 120 K to be  $\sim 13$  J/(K mol-Cr) (not shown), which roughly agrees with the theoretical value  $R\ln 4 = 11.5$  J/(K mol-Cr) for the  $S = 3/2$  spin system. Notably, the thermal expansion  $\Delta L/L_{2K}$  rapidly decreases below 35 K with decreasing temperature, suggesting a significant volume contraction across  $T_N$ . This behavior is similar to  $\text{Li}(\text{Ga}, \text{In})\text{Cr}_4\text{O}_8$  [28], where a crystal symmetry lowering was observed [21, 23]. As shown below, we confirm the crystal symmetry lowering for  $\text{CuGaCr}_4\text{S}_8$  from the powder XRD measurement at low temperatures. Moreover, the dielectric constant  $\epsilon'$  exhibits a steplike anomaly at  $T_N$  [inset of Fig. 4(d)] as observed in  $\text{Li}(\text{Ga}, \text{In})\text{Cr}_4\text{O}_8$  [22, 23]. A previous powder neutron diffraction study [36] proposes that the magnetic structure below  $T_N$  is an incommensurate spiral state. Thus, the observed dielectric anomaly would be of magnetic origin; in other words,  $\text{CuGaCr}_4\text{S}_8$  would be a type-II multi-

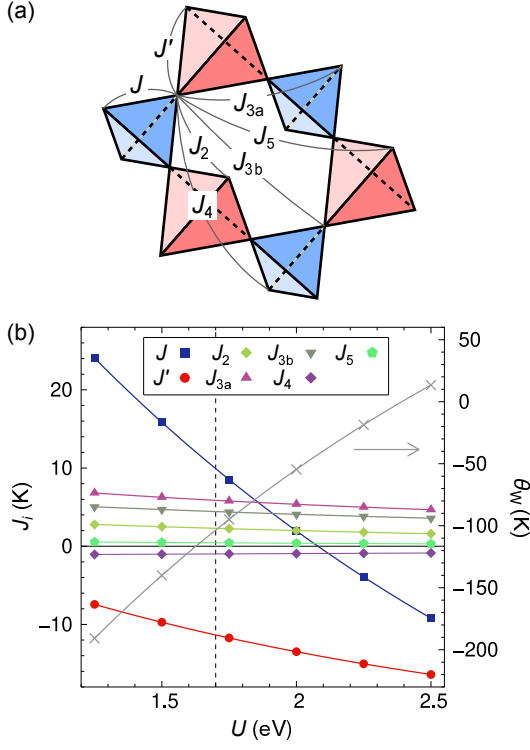


FIG. 6. (a) Definition of the exchange couplings up to the fifth-NN path in the breathing pyrochlore lattice. (b) Exchange parameters of  $\text{CuGaCr}_4\text{S}_8$  at room temperature obtained by the DFT energy mapping as function of the onsite interaction strength  $U$ . The corresponding Weiss temperature is denoted by crosses in the right axis. The vertical line indicates the  $U$  value where the exchange couplings match the experimental Weiss temperature  $\Theta_W = -103$  K.

ferroic [54].

To reveal the structural change across the magnetic transition, we investigate the powder XRD patterns at low temperatures. Figure 5 shows the temperature evolution of peak profile of some Bragg reflections. Peak splitting is clearly observed for many reflections below  $T_N$ , signaling that the magnetic transition accompanies a structural transition. We note that the peak splitting was not observed in the previous powder neutron diffraction study [36] because the expected splitting is much smaller than the experimental peak width,  $\sim 0.2^\circ$  and  $\sim 2^\circ$ , respectively, which is not sufficient to resolve the symmetry lowering below  $T_N$ . Remarkably,  $hhh$  reflections split into two peaks whereas no splitting or broadening is observed for  $h00$  reflections [Figs. 5(b) and 5(c)]. These observations can be accounted for by rhombohedral distortion, as opposed to tetragonal or orthorhombic distortion in other Cr spinels [21, 23, 55–58]. However, the proposed magnetic modulation vector  $\mathbf{Q} = (0.18, 0, 0.80)$  [36] may not directly cause rhombohedral distortion, but is compatible with monoclinic distortion. Indeed, the peak profile of 440 reflection below  $T_N$  can be well fitted by the superposition of three Lorentzian functions rather than two [see Fig. 5(a) and Appendix B]. This suggests that the crystal symmetry below  $T_N$  is lower than rhombohedral. More detailed crystallographic

TABLE II. Exchange couplings up to third-NN in four kinds of A-site-ordered Cr thiospinels estimated by the DFT energy mapping.

	$J/k_B$	$J'/k_B$	$J_2/k_B$	$J_{3a}/k_B$	$J_{3b}/k_B$	Ref.
$\text{LiGaCr}_4\text{S}_8$	-7.7 K	-12.2 K	1.2 K	6.1 K	3.0 K	[18]
$\text{LiInCr}_4\text{S}_8$	-0.3 K	-28.0 K	0.7 K	5.3 K	2.4 K	[18]
$\text{CuGaCr}_4\text{S}_8$	9.8 K	-11.4 K	2.3 K	5.9 K	4.4 K	This work
$\text{CuInCr}_4\text{S}_8$	14.7 K	-26.0 K	1.1 K	6.4 K	4.5 K	[18]

and magnetic structure analysis is necessary to settle the issue.

### C. DFT energy mapping

Based on the A-site-ordered crystal structure at room temperature shown in Table I, we performed the DFT calculations to estimate the exchange couplings of  $\text{CuGaCr}_4\text{S}_8$ . More details of the calculations are found in Appendix C. Figure 6(b) shows the DFT energy mapping up to the fifth-NN exchange couplings, which are defined in the Heisenberg Hamiltonian of the form  $\mathcal{H} = \sum_{i<j} J_{ij} \mathbf{S}_i \cdot \mathbf{S}_j$  [see Fig. 6(a)]. Exchange interactions monotonically evolve with onsite Coulomb interaction strength  $U$ . The vertical dashed line indicates the  $U$  value for which the exchange couplings match the experimental Weiss temperature of  $\Theta_W = -103$  K (see also Appendix A). The obtained parameter set is  $J/k_B = 9.8(7)$  K,  $J'/k_B = -11.4(6)$  K,  $J_2/k_B = 2.3(5)$  K,  $J_{3a}/k_B = 5.9(3)$  K,  $J_{3b}/k_B = 4.4(3)$  K,  $J_4/k_B = -1.0(3)$  K, and  $J_5/k_B = 0.4(3)$  K, where  $k_B$  is the Boltzmann's constant, representing that  $\text{CuGaCr}_4\text{S}_8$  is characterized by strong AFM  $J$  and FM  $J'$ . Since the strengths of the exchange couplings should be modified below  $T_N$  due to the lower-symmetry crystal structure, the ground state cannot be simply represented by these parameters. Nevertheless, our magnetization measurements suggest that the low-temperature magnetism of  $\text{CuGaCr}_4\text{S}_8$  can be understood based on the AFM- $J$ -FM- $J'$  picture, as discussed in Sec. IV A.

Table II compares the exchange parameters among four kinds of A-site-ordered Cr thiospinels estimated in the previous works [18] and this work. One can find that  $J$  and  $J'$  are strongly dependent on the types of nonmagnetic cations. The occupation of Li atoms at the 4a site leads to FM  $J$ , whereas that of Cu atoms leads to AFM  $J$ .  $J'$  is always FM, and its strength is enhanced when In atoms occupy the 4d site. These tendencies are reasonable because monovalent  $A^+$  (trivalent  $A^{3+}$ ) cations are surrounded by S1 (S2) atoms connecting the short (long) NN Cr–Cr bonds [Fig. 1(b)]. The Hamiltonian of  $\text{CuGaCr}_4\text{S}_8$  is qualitatively similar to that of  $\text{CuInCr}_4\text{S}_8$  except that  $|J'|$  is much smaller. In other words, the effects of further-neighbor interactions, especially  $J_{3a}$  and  $J_{3b}$ , are more important for  $\text{CuGaCr}_4\text{S}_8$  than for  $\text{CuInCr}_4\text{S}_8$ . This may be responsible for the difference in the ground state at zero field; a commensurate  $\mathbf{Q} = (1, 0, 0)$  state with an  $S = 6$  spin cluster in the large tetrahedron is realized for  $\text{CuInCr}_4\text{S}_8$  [30], whereas an incommensurate spiral state in which four spins in the large tetrahedra are not parallel with each other

TABLE III. Critical fields of the successive phase transitions in  $\text{CuGaCr}_4\text{S}_8$  and  $\text{CuInCr}_4\text{S}_8$  at  $\sim 5$  K.  $H_{c0}$  indicates a spin-flop transition in a low-field region observed only for  $\text{CuGaCr}_4\text{S}_8$ .  $H_{c1} \sim H_{c3}$  correspond to the termination fields of X, Y, and C phases, which can be assigned to canted 2:2, canted 2:1:1, and 3-up-1-down phases, respectively, based on the magnetoelastic theory [27].  $H_{\text{sat}}$  indicates the expected saturation field deduced from Eq. (2) ( $J'$ : FM) using the exchange couplings based on the DFT calculations [18].

	$\mu_0 H_{c0}$	$\mu_0 H_{c1}$	$\mu_0 H_{c2}$	$\mu_0 H_{c3}$	$\mu_0 H_{\text{sat}}$	Ref.
$\text{CuGaCr}_4\text{S}_8$	10.8 T	40.4 T	42.1 T	103 T	170 T	This work
$\text{CuInCr}_4\text{S}_8$	—	32 T	56 T	112 T	180 T	[27, 32]

for  $\text{CuGaCr}_4\text{S}_8$  [36].

#### IV. MAGNETIC-FIELD INDUCED PHASE TRANSITIONS

##### A. Magnetization curves

We here move on to the field-induced properties of  $\text{CuGaCr}_4\text{S}_8$  revealed by pulsed high-field experiments. Figure 7(a) shows magnetization curves measured at various initial temperatures  $T_{\text{ini}}$  using the ND pulsed magnet. Although they appear simple at a glance, anomalies in the field derivatives  $dM/dH$  show a complicated temperature dependence, as shown in Fig. 7(b). For  $T_{\text{ini}} = 4.2$  K, a drastic magnetization jump is observed at around 40 T accompanied by a large hysteresis, where  $dM/dH$  exhibits a sharp peak at  $\mu_0 H_{c1} = 40.4$  T and a shoulder-like anomaly at  $\mu_0 H_{c2} = 42.1$  T in the field-increasing process. The shoulder-like anomaly does not change its position while the peak moves to a lower field at 37.4 T in the field-decreasing process. After the metamagnetic transition,  $M$  reaches  $\sim 1.2 \mu_B/\text{Cr}$ , which is much smaller than the expected saturation value of  $\sim 3 \mu_B/\text{Cr}$ . As  $T_{\text{ini}}$  increases,  $H_{c1}$  shifts to a lower field and the hysteresis becomes smaller. Notably, a broad shoulder-like structure appears on the low-field side of the  $dM/dH$  peak at  $H'_{c1}$ , as denoted by open triangles in Fig. 7(b). As shown in Sec. IV B, this magnetization anomaly is accompanied by a pronounced dielectric response. Even for  $T_{\text{ini}} = 36$  K ( $> T_N$ ), a weak metamagnetic transition from the paramagnetic phase is observed at  $\mu_0 H_p = 38.3$  T, indicating that the field-induced phase is robust against thermal fluctuations.

For all the measured  $T_{\text{ini}}$ 's below  $T_N$ , a subtle slope change in the magnetization curve is observed at  $\mu_0 H_{c0} \approx 10$  T, which is visible as a  $dM/dH$  cusp [inset of Fig. 7(b)]. This phase transition is also confirmed by the magnetization measurement up to 14 T in a static magnetic field (see Fig. 11 in Appendix D). We ascribe these anomalies to a spin-flop transition with the reorientation of magnetic domains of the helical state, as observed for  $\text{CdCr}_2\text{O}_4$  [59–63]. For  $T_{\text{ini}} = 1.4$  K,  $dM/dH$  exhibits two peaks around 40 T in the field-increasing process [Fig. 7(b)]. We tentatively view this behavior as a splitting of the peak at  $H_{c1}$  observed for  $T_{\text{ini}} \geq 4.2$  K, though its origin is unclear at present.

To get a whole picture of the field-induced phase transi-

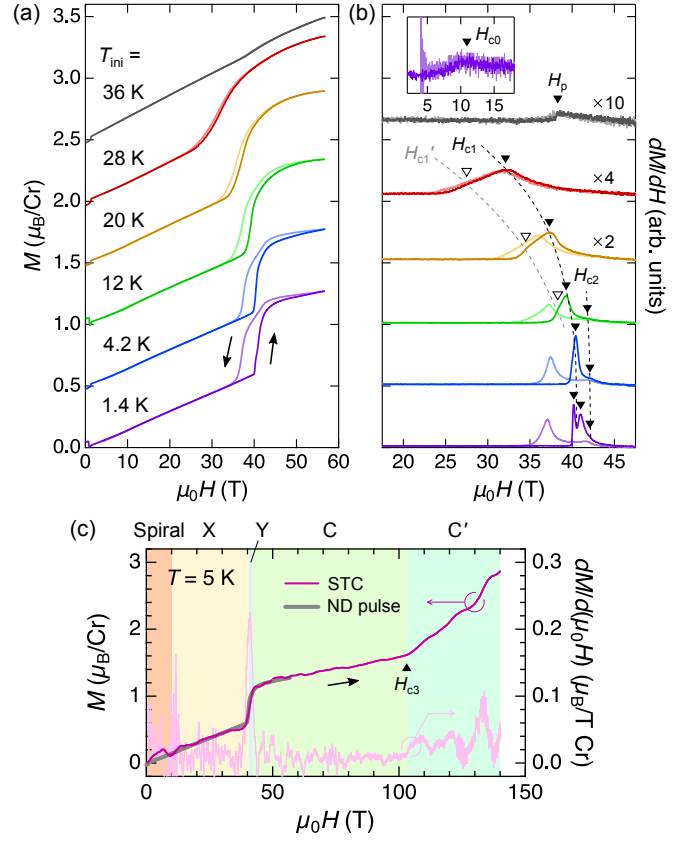


FIG. 7. (a)(b) Magnetic-field dependence of (a) magnetization  $M$  and (b) its field derivative  $dM/dH$  measured at various initial temperatures  $T_{\text{ini}}$  in a non-destructive (ND) pulsed magnet. Thick (thin) lines correspond to the data in field-increasing (decreasing) processes. The curves except for  $T_{\text{ini}} = 1.4$  K are shifted upward for clarity. The inset of (b) is an enlarged view of  $dM/dH$  around the lowest-field phase transition for  $T_{\text{ini}} = 1.4$  K. (c) Magnetic-field dependence of  $M$  (left) and  $dM/dH$  (right) in the field-increasing process measured at  $T_{\text{ini}} \sim 5$  K in a single-turn-coil (STC) system. The absolute value of  $M$  is calibrated by fitting with the  $M$ - $H$  curve for  $T_{\text{ini}} = 4.2$  K obtained in a ND pulsed magnet (gray).

tions, we further measure the magnetization at  $T_{\text{ini}} \sim 5$  K up to  $\sim 140$  T using the STC system. As shown in Fig. 7(c), a plateau-like behavior is observed between  $\mu_0 H_{c1} = 40$  T and  $\mu_0 H_{c3} = 103$  T in the field-increasing process. Note that the transition at  $H_{c2}$  is not resolved due to an electromagnetic noise. Judging from the magnitude of  $M$  in this field range ( $\sim 1.5 \mu_B/\text{Cr}$ ), a 3-up-1-down state with a 1/2-magnetization plateau is expected to appear as in Cr spinel oxides [26, 55, 64–68] and  $\text{CuInCr}_4\text{S}_8$  [27]. Above  $H_{c3}$ ,  $M$  rapidly increases up to the applied maximum field of 140 T, where  $M$  reaches  $\sim 2.8 \mu_B/\text{Cr}$ . This indicates that the saturation field  $H_{\text{sat}}$  is a bit higher than 140 T.

Theoretically, AFM- $J$ -AFM- $J'$  or AFM- $J$ -FM- $J'$  breathing pyrochlore magnets with the spin-lattice coupling can host a 1/2-magnetization plateau [11, 27]. If we consider the mean-field approximation and neglect the spin-lattice coupling,  $\Theta_W$

and  $H_{\text{sat}}$  are related to the exchange couplings as

$$-\frac{S(S+1)}{k_B} \Theta_W = J + J' + \bar{J}_{\text{AFM}} + \bar{J}_{\text{FM}} \quad (1)$$

and

$$\frac{g\mu_B}{4S} \mu_0 H_{\text{sat}} = \begin{cases} J + J' + \bar{J}_{\text{AFM}} & (J' : \text{AFM}) \\ J + \bar{J}_{\text{AFM}} & (J' : \text{FM}), \end{cases} \quad (2)$$

where  $\bar{J}_{\text{AFM}}$  and  $\bar{J}_{\text{FM}}$  are the summation of AFM and FM further-neighbor exchange couplings, respectively, and  $g \approx 2.1$  is the Landé  $g$  factor estimated from the Curie-Weiss fit [Fig. 3(a)]. For  $\text{CuGaCr}_4\text{S}_8$ , if we assume AFM- $J$ -AFM- $J'$  and  $\bar{J}_{\text{FM}} \approx 0$ , the saturation field is estimated to  $\mu_0 H_{\text{sat}} \approx 117$  T. This value is significantly underestimated compared to the experimentally expected value ( $> 140$  T), ensuring that the AFM- $J$ -FM- $J'$  picture is appropriate, as suggested by the DFT calculations (Sec. III A). If we substitute the exchange parameters shown in Table II into Eq. (2), where  $\bar{J}_{\text{AFM}} = 4J_2 + 2J_{3a} + 2J_{3b} + 2J_5$  and  $\bar{J}_{\text{FM}} = 2J_4$ , the saturation field is estimated to  $\mu_0 H_{\text{sat}} \approx 170$  T. This seems to be in good agreement with the experimental magnetization curve at 5 K [Fig. 7(c)], given that  $H_{\text{sat}}$  would be suppressed by the spin-lattice coupling and thermal fluctuations.

The overall magnetization curve of  $\text{CuGaCr}_4\text{S}_8$  at 4.2 or 5 K is similar to that of  $\text{CuInCr}_4\text{S}_8$  [27, 32]. For both the compounds, an intermediate-field phase appears just below the 1/2-magnetization plateau. The magnetic structure in the intermediate-field phase is expected to be a canted 2:1:1 state according to the magnetoelastic theory assuming the effective  $S = 6$  FCC-lattice model [27], which predicts successive phase transitions from a canted 2:2 to canted 2:1:1, 3-up-1-down, canted 3:1, and a fully polarized phase. Note that a canted 2:1:1 phase is also observed for  $\text{ZnCr}_2\text{O}_4$  [65] and  $\text{MgCr}_2\text{O}_4$  [66] in a narrow field range. An incommensurate spiral component would coexist in the canted spin states in  $\text{CuGaCr}_4\text{S}_8$  due to the presence of sizable further-neighbor exchange couplings and/or the DM interaction, as proposed for  $\text{CdCr}_2\text{O}_4$  [59, 62]. In the following, we call the field-induced phases of  $\text{CuGaCr}_4\text{S}_8$  at 5 K X, Y, C, and C' phases in the ascending order of the field [Fig. 7(c)]. Table III summarizes the critical field of each phase transition in the field-increasing process for  $\text{CuGaCr}_4\text{S}_8$  and  $\text{CuInCr}_4\text{S}_8$  [27, 32]. Theoretically, as the SLC gets stronger, the 1/2-magnetization plateau expands while the canted 2:1:1 phase gets narrower [27]. Considering  $H_{c3}/H_{c2} \sim 2.5$  and 2.0 for  $\text{CuGaCr}_4\text{S}_8$  and  $\text{CuInCr}_4\text{S}_8$ , respectively, it can be said that the 3-up-1-down state is more stable in  $\text{CuGaCr}_4\text{S}_8$  than in  $\text{CuInCr}_4\text{S}_8$ . Besides, the field range between  $H_{c1}$  and  $H_{c2}$  (Y phase) is much narrower in  $\text{CuGaCr}_4\text{S}_8$  than in  $\text{CuInCr}_4\text{S}_8$ . These trends suggest that the SLC is stronger in  $\text{CuGaCr}_4\text{S}_8$  than in  $\text{CuInCr}_4\text{S}_8$ . The strong SLC in  $\text{CuGaCr}_4\text{S}_8$  is consistent with the observation of a first-order phase transition at  $T_N$ .

### B. Magnetostrictive and magnetodielectric effects

Figure 8(a) shows the field dependence of the longitudinal magnetostriction and the longitudinal dielectric constant,

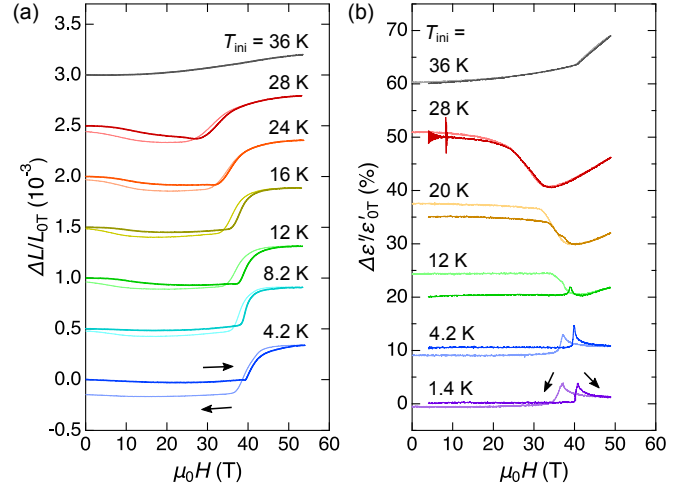


FIG. 8. Magnetic-field dependence of relative changes in (a) the sample length along the field direction  $\Delta L/L_{0T}$  and (b) dielectric constant  $\Delta\epsilon'/\epsilon'_{0T}$  measured at various initial temperatures  $T_{\text{ini}}$ . Data presentation is the same as Fig. 7.

respectively, measured on a sintered sample at various  $T_{\text{ini}}$ 's using the ND pulsed magnet. Here,  $\Delta L/L_{0T}$  and  $\Delta\epsilon'/\epsilon'_{0T}$  represent the relative changes normalized by the zero-field values at each  $T_{\text{ini}}$ . For  $T_{\text{ini}} = 36$  K,  $\Delta L/L_{0T}$  shows a parabolic field dependence at low fields as expected in the paramagnetic state. For  $T_{\text{ini}}$  below  $T_N$ , on the other hand,  $\Delta L/L_{0T}$  remains almost constant or exhibits negative magnetostriction in the spiral phase and X phase. This tendency is in contrast to  $\text{Li}(\text{Ga}, \text{In})\text{Cr}_4\text{S}_8$  [28] and  $\text{CuInCr}_4\text{S}_8$  [32], where  $\Delta L/L_{0T}$  gradually increases with respect to a magnetic field. A slight slope change at around 10 T observed for  $12 \leq T_{\text{ini}} \leq 28$  K would reflect the spin-flop transition at  $H_{c0}$ . On entering the 1/2-magnetization plateau above  $H_{c1}$ , a drastic lattice expansion is observed in analogy with other Cr spinels [32, 61, 69], suggesting that the 3-up-1-down collinear state is stabilized by the exchange striction.

Interestingly, diverse dielectric responses are observed as shown in Fig. 8(b). For  $T_{\text{ini}} = 1.4$  and 4.2 K,  $\Delta\epsilon'/\epsilon'_{0T}$  shows a sharp peak with a magnitude of  $\sim 4\%$  between X and Y phases at  $H_{c1}$ . As  $T_{\text{ini}}$  increases toward  $T_N$ , the dielectric anomaly around  $H_{c1}$  transforms into a broad valley shape with a reduction of as large as  $\sim 8\%$ . For  $T_{\text{ini}} = 12$  K, a valley structure is seen only in the field-decreasing process, presumably suggesting that the actual sample temperature would be higher than  $T_{\text{ini}}$  in the field-decreasing process due to the magnetocaloric effect [32, 70]. Of particular note is the 20-K data, in which a tiny  $\Delta\epsilon'/\epsilon'$  peak coexist with the valley structure. This supports the occurrence of another phase transition other than that from X to Y phase, as suggested by the magnetization data [Fig. 7(b)]. We hereafter call the additional higher-temperature phase “Z phase”.

The magnetoelectric effect of the A-site-ordered spinel has long been a subject of interest in view of the inversion symmetry breaking of the crystal structure [71, 72]. However, the reported dielectric anomalies associated with magnetic transitions are weak for  $\text{Li}(\text{Ga}, \text{In})\text{Cr}_4\text{O}_8$  [22, 23], where a collinear



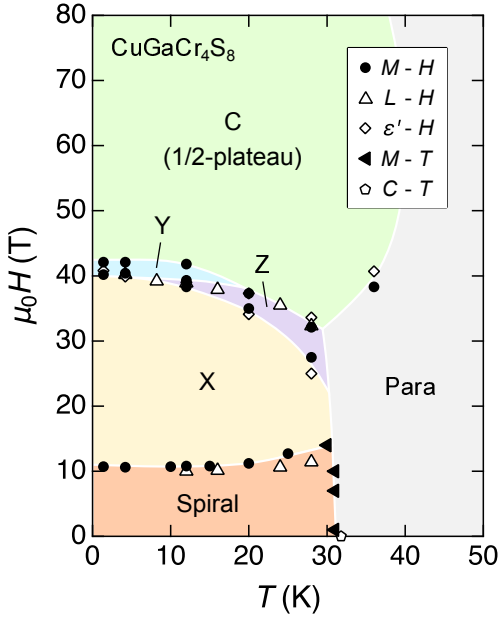


FIG. 9.  $H$ - $T$  phase diagram of CuGaCr<sub>4</sub>S<sub>8</sub> based on physical property measurements performed in the present work. Note that another high-field phase ( $C'$  phase) appears above  $\mu_0 H_{c3} = 103$  T at  $\sim 5$  K. According to the magnetoelastic theory [27], the magnetic structure of  $C$  phase is expected to be a 3-up-1-down state.

2-up-2-down magnetic LRO is induced by the SLC at low temperatures. We stress that the observed dielectric anomaly in CuGaCr<sub>4</sub>S<sub>8</sub> is much larger than in the oxide cases thanks to the emergence of incommensurate magnetic LROs [36]. A single-crystal study on CuGaCr<sub>4</sub>S<sub>8</sub> would be a promising route to seek for significant electric polarization changes.

### C. $H$ - $T$ phase diagram

Based on a series of physical property measurements, we construct an  $H$ - $T$  phase diagram of CuGaCr<sub>4</sub>S<sub>8</sub>, as shown in Fig. 9. As discussed in Sec. IV A, the magnetic structures of  $X$ ,  $Y$ ,  $C$  phases are possibly canted 2:2, canted 2:1:1, and 3-up-1-down states, respectively, based on the magnetoelastic theory [27], though in reality an incommensurate spiral component would coexist with the commensurate collinear component. We also observe a weak spin-flop transition at around 10 T, so that the  $X$  phase may be just a flopped spiral state with  $\mathbf{Q} = (0.18, 0, 0.80)$  [36]. An additional magnetization measurement using the STC system reveals that the  $C$  phase terminates at  $\mu_0 H_{c3} = 103$  T, followed by the  $C'$  phase with a possible canted 3:1 state up to at least 140 T at  $\sim 5$  K.

The identified magnetic phase diagram is basically shared with those of Cr spinel oxides [55, 61, 64–66, 70] and CuInCr<sub>4</sub>S<sub>8</sub> [27, 32] where a robust 1/2-magnetization plateau ( $C$  phase) intervenes between spin-canted phases on lower- and higher-field sides. A characteristic feature of CuGaCr<sub>4</sub>S<sub>8</sub> is the appearance of a field-induced high-temperature phase ( $Z$  phase) immediately below the  $C$  phase, in common

with another AFM- $J$ -FM- $J'$  breathing pyrochlore compound CuInCr<sub>4</sub>S<sub>8</sub>, which hosts an  $A$  phase in a closed  $H$ - $T$  regime around 25–40 T and 10–35 K [32]. In the case of CuInCr<sub>4</sub>S<sub>8</sub>, the appearance of the  $A$  phase is accompanied by negative magnetostriction and the enhancement of magnetocapacitance at a lower phase boundary [32]. These features are not the case for the  $Z$  phase in CuGaCr<sub>4</sub>S<sub>8</sub>. Thus, we infer that the  $Z$  phase in CuGaCr<sub>4</sub>S<sub>8</sub> is different from the  $A$  phase in CuInCr<sub>4</sub>S<sub>8</sub>. The identification of these field-induced high-temperature phases in AFM- $J$ -FM- $J'$  breathing pyrochlore systems would be an intriguing issue left for future works.

## V. SUMMARY

We synthesized CuGaCr<sub>4</sub>S<sub>8</sub> polycrystalline samples and demonstrated the formation of a breathing pyrochlore Cr network by the synchrotron XRD measurement and the Rietveld analysis. The DFT energy mapping suggests that the spin Hamiltonian is characterized by AFM  $J$ , FM  $J'$ , and relatively strong further-neighbor exchange couplings, so that the system harbors both geometrical frustration and bond frustration. Remarkably, the comparison of exchange parameters among four AA'Cr<sub>4</sub>S<sub>8</sub> compounds (Table II) provides insights into the relationship between the chemical composition and the spin Hamiltonian in breathing pyrochlore chromium thiospinels. We also unveil diverse magnetic phases associated with prominent magnetostrictive and magnetodielectric effects at low temperatures and in high magnetic fields. These observations in CuGaCr<sub>4</sub>S<sub>8</sub> could be attributed to the magnetic frustration and strong SLC, highlighting the complex interplay of these factors.

## ACKNOWLEDGEMENTS

We appreciate Y. Okamoto, M. Mori, and S. Kitou for helpful discussions. This work was financially supported by the Japan Society for the Promotion of Science (JSPS) KAKENHI Grants-In-Aid for Scientific Research (No. 20J10988). M.G. was a postdoctoral research fellow of the JSPS.

### Appendix A: Rietveld analysis assuming various structural models

Here, we show the results of the Rietveld analysis assuming several types of structural models. Basically, the normal spinel structure with the  $Fd\bar{3}m$  space group, in which Cu and Ga atoms are randomly distributed at the  $8a$  site with an occupancy of 0.5, yields satisfactory refinement with relatively small reliability factors, as shown in Fig. 10 and Table IV. However, upon relaxing the constraint on the atomic position of Cr,  $x(\text{Cr})$ , while maintaining the random distribution of Cu and Ga and the atomic position of S,  $x(\text{Cr})$  tends to deviate from 0.375, suggesting that the  $F\bar{4}3m$  space group is more likely. Such symmetry lowering should originate from the crystallographic ordering of Cu<sup>+</sup> and Ga<sup>3+</sup> with different ionic



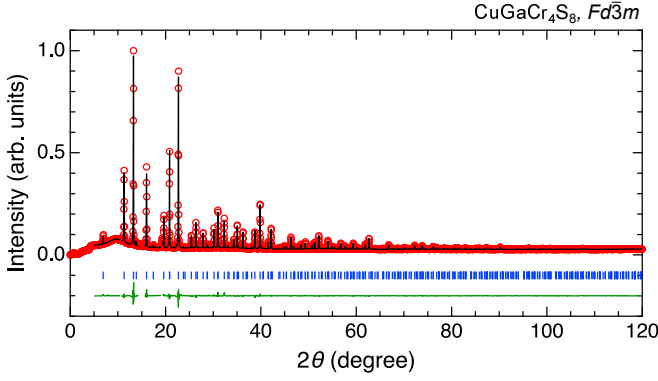


FIG. 10. Rietveld refinement on the synchrotron XRD pattern based on the  $Fd\bar{3}m$  space group.

radii (0.60 Å and 0.47 Å, respectively, in the four-fold coordination). Accordingly, we consider two types of perfectly A-site-ordered structures with  $x(\text{Cr}) < 0.375$ : Cu (Ga) occupies the  $4a$  ( $4d$ ) site for type #1, whereas Cu (Ga) occupies the  $4d$  ( $4a$ ) site for type #2. Note that there can be two inequivalent atomic sites of S for the  $F\bar{4}3m$  space group [3, 24, 31]. The refinement results for the type #1 and #2 structures are shown in Tables I and V, respectively. In the both refinements, the reliability factors are smaller compared to the case of the  $Fd\bar{3}m$  model. Although the resultant structural parameters are almost the same within errors between type #1 and #2, the thermal parameter of Ga is unusually large for type #2, suggesting that type #1 is more reasonable. This is further supported by the calculation of DFT total energies; type #1 is 293 meV per formula unit lower in energy than type #2.

#### Appendix B: Lorentzian fit on the peak profile of 440 reflection at low temperatures

Figure 11 shows an enlarged view of the powder XRD pattern of  $\text{CuGaCr}_4\text{S}_8$  around the 440 reflection at 4 K. This peak can be fitted by the superposition of three Lorentzian functions with peak positions of 52.08°, 52.19°, and 52.34°.

TABLE IV. Structural parameters of  $\text{CuGaCr}_4\text{S}_8$  at room temperature assuming the  $Fd\bar{3}m$  space group, where Cu and Ga atoms are randomly distributed at the  $8a$  site with an occupancy of 0.5. The lattice constant is  $a = 9.91910(9)$  Å. Reliability factors are  $R_{\text{wp}} = 2.967$ ,  $R_{\text{p}} = 1.897$ ,  $R_{\text{e}} = 1.706$ ,  $S = 1.7390$ .

		$x$	$y$	$z$	Occup.	B (Å)
Cu	$8a$	0	0	0	0.5	0.80(2)
Ga	$8a$	0	0	0	0.5	0.80(2)
Cr	$16d$	0.375	$x$	$x$	1	0.85(2)
S	$32e$	0.38382(6)	$x$	$x$	1	0.61(2)

TABLE V. Structural parameters of  $\text{CuGaCr}_4\text{S}_8$  at room temperature assuming the  $F\bar{4}3m$  space group, where Cu and Ga atoms occupy the  $4d$  and  $4a$  sites, respectively, and the atomic position  $x$  of Cr is less than 0.375. The lattice constant is  $a = 9.92035(8)$  Å. Reliability factors are  $R_{\text{wp}} = 2.838$ ,  $R_{\text{p}} = 1.773$ ,  $R_{\text{e}} = 1.711$ ,  $S = 1.6588$ .

		$x$	$y$	$z$	Occup.	B (Å)
Cu	$4d$	3/4	3/4	3/4	1	0.69(6)
Ga	$4a$	0	0	0	1	1.00(7)
Cr	$16e$	0.37041(14)	$x$	$x$	1	0.64(2)
S1	$16e$	0.13340(22)	$x$	$x$	1	0.79(4)
S2	$16e$	0.61683(17)	$x$	$x$	1	0.62(4)

#### Appendix C: Details of the DFT energy mapping

Our DFT calculations are performed using the all electron full potential FPLO code [46]. We create a  $2 \times 2 \times 1$  supercell with  $Pm$  symmetry and twelve symmetry inequivalent  $\text{Cr}^{3+}$  ions. This allows us to go slightly beyond the minimal set of exchange interactions  $J$ ,  $J'$ ,  $J_2$ ,  $J_{3a}$ , and  $J_{3b}$ , which is known to describe the breathing pyrochlore thiospinels well [18, 27]; we also resolve  $J_4$  which has been shown to noticeably affect the inelastic neutron spectrum of  $\text{CuInCr}_4\text{S}_8$  [30] and  $\text{ZnCr}_2\text{Se}_4$  [73]. We calculate 30 spin configurations and fit them with the classical Heisenberg Hamiltonian energies; the good quality of the fit is shown in Fig. 12. We select the onsite interactions strength  $U$  which is suitable for the description of  $\text{CuGaCr}_4\text{S}_8$  by calculating the Weiss temperature for the obtained exchange interactions via Eq. (1), where  $\bar{J}_{\text{AFM}} = 4J_2 + 2J_{3a} + 2J_{3b} + 2J_5$  and  $\bar{J}_{\text{FM}} = 2J_4$ . For an interpolated  $U = 1.70$  eV, the set of couplings exactly matches the experimental value  $\Theta_{\text{W}} = -103$  K. This  $U$  value falls into the range of  $U$  values  $1.4 \text{ eV} < U < 2.0 \text{ eV}$  that describe many other chromium spinels [18].

#### Appendix D: Low-field phase transition observed in a static magnetic field

Figure 13 shows the magnetization curves measured at various temperatures using a vibrating sample magnetometer in

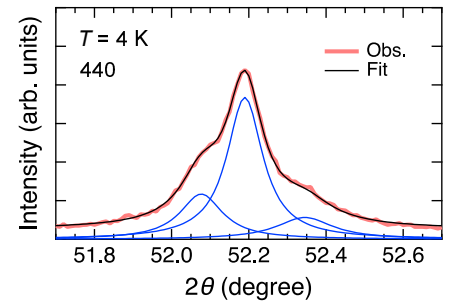


FIG. 11. Multi-Lorentzian fit (black) to the peak profile of 440 reflection at 4 K (pink), which is obtained by the superposition of three Lorentzian functions (blue).

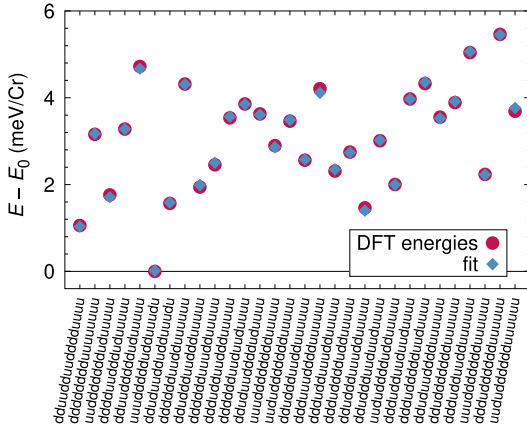


FIG. 12. DFT energies of  $\text{CuGaCr}_4\text{S}_8$ , calculated within GGA+ $U$  at  $J_H = 0.72$  eV,  $U = 1.70$  eV and  $6 \times 6 \times 6$   $k$  points in a  $2 \times 2 \times 1$  supercell for 30 different spin configurations, compared with a fit to the Heisenberg model. The good fit indicates that the extracted exchange interactions represent the magnetic properties of  $\text{CuGaCr}_4\text{S}_8$  well.

a PPMS. A cusp structure is clearly observed in the  $dM/dH$  data below 25 K, indicating a spin-flop transition. The transition field  $H_{c0}$  gradually increases as the temperature increases.

This trend is in line with the typical  $H$ - $T$  phase diagram of the spin-flop transition in antiferromagnets.

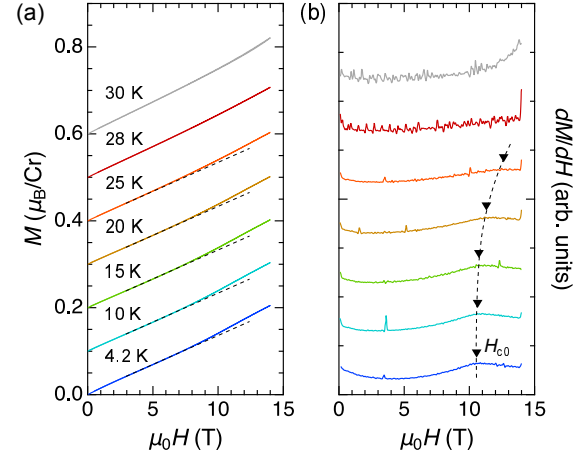


FIG. 13. Magnetic-field dependence of (a) magnetization  $M$  and (b) its field derivative  $dM/dH$  measured at various temperatures in a static magnetic field. The curves except for 4.2 K are shifted upward for clarity. Dashed lines in (a) are guides to the eye to make it easier to see the slope change in the  $M$ - $H$  curves.

- [1] J. S. Gardner, M. J. P. Gingras, and J. E. Greedan, Magnetic pyrochlore oxides, *Rev. Mod. Phys.* **82**, 53 (2010).
- [2] D. Reig-i-Plessis and A. M. Hallas, Frustrated magnetism in fluoride and chalcogenide pyrochlore lattice materials, *Phys. Rev. Mater.* **5**, 030301 (2021).
- [3] Y. Okamoto, G. J. Nilsen, J. P. Attfield, and Z. Hiroi, Breathing Pyrochlore Lattice Realized in A-Site Ordered Spinel Oxides  $\text{LiGaCr}_4\text{O}_8$  and  $\text{LiInCr}_4\text{O}_8$ , *Phys. Rev. Lett.* **110**, 097203 (2013).
- [4] O. Benton and N. Shannon, Ground State Selection and Spin-Liquid Behaviour in the Classical Heisenberg Model on the Breathing Pyrochlore Lattice, *J. Phys. Soc. Jpn.* **84**, 104710 (2015).
- [5] L. Savary, X. Wang, H.-Y. Kee, Y. B. Kim, Y. Yu, and G. Chen, Quantum spin ice on the breathing pyrochlore lattice, *Phys. Rev. B* **94**, 075146 (2016).
- [6] F.-Y. Li, Y.-D. Li, Y. B. Kim, L. Balents, Y. Yu, and G. Chen, Weyl magnons in breathing pyrochlore antiferromagnets, *Nat. Commun.* **7**, 12691 (2016).
- [7] Y. Iqbal, T. Müller, P. Ghosh, M. J. P. Gingras, H. O. Jeschke, S. Rachel, J. Reuther, and R. Thomale, Quantum and Classical Phases of the Pyrochlore Heisenberg Model with Competing Interactions, *Phys. Rev. X* **9**, 011005 (2019).
- [8] H. Yan, O. Benton, L. D. C. Jaubert, and N. Shannon, Rank-2  $U(1)$  Spin Liquid on the Breathing Pyrochlore Lattice, *Phys. Rev. Lett.* **124**, 127203 (2020).
- [9] S. E. Han, A. S. Patri, and Y. B. Kim, Realization of fractional quantum phases in the breathing pyrochlore lattice, *Phys. Rev. B* **105**, 235120 (2022).
- [10] K. Aoyama and H. Kawamura, Spin ordering induced by lattice distortions in classical Heisenberg antiferromagnets on the breathing pyrochlore lattice, *Phys. Rev. B* **99**, 144406 (2019).
- [11] K. Aoyama, M. Gen, and H. Kawamura, Effects of spin-lattice coupling and a magnetic field in classical Heisenberg antiferromagnets on the breathing pyrochlore lattice, *Phys. Rev. B* **104**, 184411 (2021).
- [12] K. Aoyama and H. Kawamura, Hedgehog-lattice spin texture in classical Heisenberg antiferromagnets on the breathing pyrochlore lattice, *Phys. Rev. B* **103**, 014406 (2021).
- [13] K. Aoyama and H. Kawamura, Hedgehog lattice and field-induced chirality in breathing-pyrochlore Heisenberg antiferromagnets, *Phys. Rev. B* **106**, 064412 (2022).
- [14] K. Kimura, S. Nakatsuji, and T. Kimura, Experimental realization of a quantum breathing pyrochlore antiferromagnet, *Phys. Rev. B* **90**, 060414(R) (2014).
- [15] T. Haku, K. Kimura, Y. Matsumoto, M. Soda, M. Sera, D. Yu, R. A. Mole, T. Takeuchi, S. Nakatsuji, Y. Kono, T. Sakakibara, L.-J. Chang, and T. Masuda, Low-energy excitations and ground-state selection in the quantum breathing pyrochlore antiferromagnet  $\text{Ba}_3\text{Yb}_2\text{Zn}_5\text{O}_{11}$ , *Phys. Rev. B* **93**, 220407(R) (2016).
- [16] J. G. Rau, L. S. Wu, A. F. May, L. Poudel, B. Winn, V. O. Garlea, A. Huq, P. Whitfield, A. E. Taylor, M. D. Lumsden, M. J. P. Gingras, and A. D. Christianson, Anisotropic Exchange within Decoupled Tetrahedra in the Quantum Breathing Pyrochlore  $\text{Ba}_3\text{Yb}_2\text{Zn}_5\text{O}_{11}$ , *Phys. Rev. Lett.* **116**, 257204 (2016).
- [17] S. Dissanayake, Z. Shi, J. G. Rau, R. Bag, W. Steinhardt, N. P. Butch, M. Frontzek, A. Podlesnyak, D. Graf, C. Marjerrison, J. Liu, M. J. P. Gingras, and S. Haravifard, Towards understanding the magnetic properties of the breathing pyrochlore compound  $\text{Ba}_3\text{Yb}_2\text{Zn}_5\text{O}_{11}$  through single-crystal studies, *npj Quantum Materials* **7**, 77 (2022).
- [18] P. Ghosh, Y. Iqbal, T. Müller, R. Thomale, J. Reuther, M. J. P. Gingras, and H. O. Jeschke, Breathing chromium spinels: a

- showcase for a variety of pyrochlore Heisenberg Hamiltonians, *npj Quantum Mater.* **4**, 63 (2019).
- [19] J.-C. Joubert and A. Durif, *Bull. Soc. Fr. Mineral.* **89**, 26 (1966).
- [20] H. L. Pinch, M. J. Woods, and E. Lopatin, Some new mixed A-site chromium chalcogenide spinels, *Mat. Res. Bull.* **5**, 425 (1970).
- [21] G. J. Nilsen, Y. Okamoto, T. Masuda, J. Rodriguez-Carvajal, H. Mutka, T. Hansen, and Z. Hiroi, Complex magnetostructural order in the frustrated spinel  $\text{LiInCr}_4\text{O}_8$ , *Phys. Rev. B* **91**, 174435 (2015).
- [22] S. Lee, S.-H. Do, W.-J. Lee, Y. S. Choi, M. Lee, E. S. Choi, A. P. Reyes, P. L. Kuhns, A. Ozarowski, and K.-Y. Choi, Multistage symmetry breaking in the breathing pyrochlore lattice  $\text{Li}(\text{Ga}, \text{In})\text{Cr}_4\text{O}_8$ , *Phys. Rev. B* **93**, 174402 (2016).
- [23] R. Saha, F. Fauth, M. Avdeev, P. Kayser, B. J. Kennedy, and A. Sundaresan, Magnetodielectric effects in A-site cation-ordered chromate spinels  $\text{LiMCr}_4\text{O}_8$  ( $M=\text{Ga}$  and  $\text{In}$ ), *Phys. Rev. B* **94**, 064420 (2016).
- [24] Y. Okamoto, M. Mori, N. Katayama, A. Miyake, M. Tokunaga, A. Matsuo, K. Kindo, and K. Takenaka, Magnetic and Structural Properties of A-Site Ordered Chromium Spinel Sulfides: Alternating Antiferromagnetic and Ferromagnetic Interactions in the Breathing Pyrochlore Lattice, *J. Phys. Soc. Jpn.* **87**, 034709 (2018).
- [25] G. Pokharel, A. F. May, D. S. Parker, S. Calder, G. Ehlers, A. Huq, S. A. J. Kimber, H. Suriya Arachchige, L. Poudel, M. A. McGuire, D. Mandrus, and A. D. Christianson, Negative thermal expansion and magnetoelastic coupling in the breathing pyrochlore lattice material  $\text{LiGaCr}_4\text{S}_8$ , *Phys. Rev. B* **97**, 134117 (2018).
- [26] M. Gen, D. Nakamura, Y. Okamoto, and S. Takeyama, Ultrahigh magnetic field magnetic phases up to 130 T in a breathing pyrochlore antiferromagnet  $\text{LiInCr}_4\text{O}_8$ , *J. Magn. Magn. Mater.* **473**, 387 (2019).
- [27] M. Gen, Y. Okamoto, M. Mori, K. Takenaka, and Y. Kohama, Magnetization process of the breathing pyrochlore magnet  $\text{CuInCr}_4\text{S}_8$  in ultrahigh magnetic fields up to 150 T, *Phys. Rev. B* **101**, 054434 (2020). [See also Erratum: M. Gen *et al.*, *Phys. Rev. B* **103**, 019901(E) (2021).]
- [28] T. Kanematsu, M. Mori, Y. Okamoto, T. Yajima, and K. Takenaka, Thermal Expansion and Volume Magnetostriction in Breathing Pyrochlore Magnets  $\text{LiACr}_4\text{X}_8$  ( $A=\text{Ga}, \text{In}$ ,  $X=\text{O}, \text{S}$ ), *J. Phys. Soc. Jpn.* **89**, 073708 (2020).
- [29] G. Pokharel, H. S. Arachchige, T. J. Williams, A. F. May, R. S. Fishman, G. Sala, S. Calder, G. Ehlers, D. S. Parker, T. Hong, A. Wildes, D. Mandrus, J. A. M. Paddison, and A. D. Christianson, Cluster Frustration in the Breathing Pyrochlore Magnet  $\text{LiGaCr}_4\text{S}_8$ , *Phys. Rev. Lett.* **125**, 167201 (2020).
- [30] S. Gao, A. F. May, M.-H. Du, J. A. M. Paddison, H. S. Arachchige, G. Pokharel, C. dela Cruz, Q. Zhang, G. Ehlers, D. S. Parker, D. G. Mandrus, M. B. Stone, and A. D. Christianson, Hierarchical excitations from correlated spin tetrahedra on the breathing pyrochlore lattice, *Phys. Rev. B* **103**, 214418 (2021).
- [31] S. Sharma, M. Pocrnic, B. N. Riechik, C. R. Wiebe, J. Beare, J. Gautreau, J. P. Clancy, J. P. C. Ruff, M. Pula, Q. Chen, S. Yoon, Y. Cai, and G. M. Luke, Synthesis and physical and magnetic properties of  $\text{CuAlCr}_4\text{S}_8$ : A Cr-based breathing pyrochlore, *Phys. Rev. B* **106**, 024407 (2022).
- [32] M. Gen, H. Ishikawa, A. Ikeda, A. Miyake, Z. Yang, Y. Okamoto, M. Mori, K. Takenaka, H. Sagayama, T. Kurumaji, Y. Tokunaga, T. Arima, M. Tokunaga, K. Kindo, Y. H. Matsuda, and Y. Kohama, Complex magnetic phase diagram with a small phase pocket in a three-dimensional frustrated magnet  $\text{CuInCr}_4\text{S}_8$ , *Phys. Rev. Research* **4**, 033148 (2022).
- [33] S. Mühlbauer, B. Binz, F. Jonietz, C. Pfleiderer, A. Rosch, A. Neubauer, R. Georgii, and P. Böni, Skyrmion Lattice in a Chiral Magnet, *Science* **323**, 915 (2009).
- [34] S. Seki, X. Z. Yu, S. Ishiwata, and Y. Tokura, Observation of Skyrmions in a Multiferroic Material, *Science* **336**, 198 (2012).
- [35] T. Okubo, S. Chung, and H. Kawamura, Multiple- $q$  States and the Skyrmion Lattice of the Triangular- Lattice Heisenberg Antiferromagnet under Magnetic Fields, *Phys. Rev. Lett.* **108**, 017206 (2012).
- [36] C. Wilkinson, B. M. Knapp, and J. B. Forsyth, The magnetic structure of  $\text{Cu}_{0.5}\text{Ga}_{0.5}\text{Cr}_2\text{S}_4$ , *J. Phys. C: Solid State Phys.* **9**, 4021 (1976).
- [37] Ya. A. Kesler, E. G. Zhukov, D. S. Filimonov, E. S. Polulyak, T. K. Menshchikova, V. A. Fedorov,  $\text{CuCr}_2\text{S}_4$ -Based Quaternary Cation-Substituted Magnetic Phases, *Inorg. Mater.* **41**, 914 (2005).
- [38] T. G. Aminov, E. V. Busheva, G. G. Shabunina, and V. M. Novotortsev, Magnetic Phase Diagram of Solid Solutions in the  $\text{CoCr}_2\text{S}_4$ - $\text{Cu}_{0.5}\text{Ga}_{0.5}\text{Cr}_2\text{S}_4$  System, *Russ. J. Inorg. Chem.* **63**, 519 (2018).
- [39] K. Momma and F. Izumi, VESTA 3 for three-dimensional visualization of crystal, volumetric and morphology data, *J. Appl. Crystallogr.* **44**, 1272 (2011).
- [40] F. Izumi and K. Momma, Three-Dimensional Visualization in Powder Diffraction, *Solid State Phenom.* **130**, 15 (2007).
- [41] A. Ikeda, Y. H. Matsuda, and H. Tsuda, Note: Optical filter method for high-resolution magnetostriction measurement using fiber Bragg grating under millisecond-pulsed high magnetic fields at cryogenic temperatures, *Rev. Sci. Instrum.* **89**, 096103 (2018).
- [42] A. Miyake, H. Mitamura, S. Kawachi, K. Kimura, T. Kimura, T. Kihara, M. Tachibana, and M. Tokunaga, Capacitive detection of magnetostriction, dielectric constant, and magneto-caloric effects in pulsed magnetic fields, *Rev. Sci. Instrum.* **91**, 105103 (2020).
- [43] H. Yamamoto, T. Sakakura, H. O. Jeschke, N. Kabeya, K. Hayashi, Y. Ishikawa, Y. Fujii, S. Kishimoto, H. Sagayama, K. Shigematsu, M. Azuma, A. Ochiai, Y. Noda, and H. Kimura, Quantum spin fluctuations and hydrogen bond network in the antiferromagnetic natural mineral henmilite, *Phys. Rev. Materials* **5**, 104405 (2021).
- [44] L. Heinze, H. O. Jeschke, I. I. Mazin, A. Metavitsiadis, M. Reehuis, R. Feyerherm, J.-U. Hoffmann, M. Bartkowiak, O. Prokhnenko, A. U. B. Wolter, X. Ding, V. S. Zapf, C. Corvalán Moya, F. Weickert, M. Jaime, K. C. Rule, D. Menzel, R. Valentí, W. Brenig, and S. Süllo, Magnetization process of atacamite: A case of weakly coupled  $S = 1/2$  sawtooth chains, *Phys. Rev. Lett.* **126**, 207201 (2021).
- [45] M. Hering, F. Ferrari, A. Razpopov, I. I. Mazin, R. Valentí, H. O. Jeschke, and J. Reuther, Phase diagram of a distorted kagome antiferromagnet and application to  $\gamma$ -kapellasite, *npj Comput. Mater.* **8**, 10 (2022).
- [46] K. Koepnick and H. Eschrig, Full-potential nonorthogonal local-orbital minimum-basis band-structure scheme, *Phys. Rev. B* **59**, 1743 (1999).
- [47] J. P. Perdew, K. Burke, and M. Ernzerhof, Generalized gradient approximation made simple, *Phys. Rev. Lett.* **77**, 3865 (1996).
- [48] A. I. Liechtenstein, V. I. Anisimov, and J. Zaanen, Density-functional theory and strong interactions: Orbital ordering in Mott-Hubbard insulators, *Phys. Rev. B* **52**, R5467 (1995).
- [49] T. Mizokawa and A. Fujimori, Electronic structure and orbital ordering in perovskite-type  $3d$  transition-metal oxides studied by Hartree-Fock band-structure calculations, *Phys. Rev. B* **54**, 5368 (1996).

- [50] M. Tokonami and H. Horiuchi, On the space group of spinel,  $\text{MgAl}_2\text{O}_4$ , *Acta Cryst. A* **36**, 122 (1980).
- [51] O. Steinsvoll and E. J. Samuelsen, The Space Group of Spinel Revisited, *Phys. Scr.* **24**, 57 (1981).
- [52] G. Subías, J. Garcia, M. G. Proietti, J. Blasco, H. Rennevier, J. L. Hodeau, and M. C. Sánchez, X-ray resonant scattering of  $(004n + 2)$  forbidden reflections in spinel ferrites, *Phys. Rev. B* **70**, 155105 (2004).
- [53] The present heat capacity measurement using the thermal relaxation method cannot accurately evaluate the latent heat associated with the first-order transition. Therefore, there remains certain ambiguity in the estimated  $S_N$ .
- [54] D. Khomskii, Classifying multiferroics: Mechanisms and effects, *Physics* **2**, 20 (2009).
- [55] H. Ueda, H. Mitamura, T. Goto, and Y. Ueda, Successive field-induced transitions in a frustrated antiferromagnet  $\text{HgCr}_2\text{O}_4$ , *Phys. Rev. B* **73**, 094415 (2006).
- [56] S.-H. Lee, G. Gasparovic, C. Broholm, M. Matsuda, J.-H. Chung, Y. J. Kim, H. Ueda, G. Xu, P. Zschack, K. Kakurai, H. Takagi, W. Ratcliff, T. H. Kim, and S.-W. Cheong, Crystal distortions in geometrically frustrated  $\text{ACr}_2\text{O}_4$  ( $A = \text{Zn}, \text{Cd}$ ), *J. Phys.: Condens. Matter* **19**, 145259 (2007).
- [57] F. Yokaichiya, A. Krimmel, V. Tsurkan, I. Margiolaki, P. Thompson, H. N. Bordallo, A. Buchsteiner, N. Stüßer, D. N. Argyriou, and A. Loidl, Spin-driven phase transitions in  $\text{ZnCr}_2\text{Se}_4$  and  $\text{ZnCr}_2\text{S}_4$  probed by high-resolution synchrotron x-ray and neutron powder diffraction, *Phys. Rev. B* **79**, 064423 (2009).
- [58] Ch. Kant, J. Deisenhofer, T. Rudolf, F. Mayr, F. Schrettle, A. Loidl, V. Gnezdilov, D. Wulferding and P. Lemmens, and V. Tsurkan, Optical phonons, spin correlations, and spin-phonon coupling in the frustrated pyrochlore magnets  $\text{CdCr}_2\text{O}_4$  and  $\text{ZnCr}_2\text{O}_4$ , *Phys. Rev. B* **80**, 214417 (2009).
- [59] M. Matsuda, M. Takeda, M. Nakamura, and K. Kakurai, A. Oosawa, E. Lelièvre-Berna, J.-H. Chung, H. Ueda, H. Takagi, S.-H. Lee, Spiral spin structure in the Heisenberg pyrochlore magnet  $\text{CdCr}_2\text{O}_4$ , *Phys. Rev. B* **75**, 104415 (2007).
- [60] S. Bhattacharjee, S. Zherlitsyn, O. Chiatti, A. Sytcheva, J. Wosnitzer, R. Moessner, M. E. Zhitomirsky, P. Lemmens, V. Tsurkan, and A. Loidl, Interplay of spin and lattice degrees of freedom in the frustrated antiferromagnet  $\text{CdCr}_2\text{O}_4$ : High-field and temperature-induced anomalies of the elastic constants, *Phys. Rev. B* **83**, 184421 (2011).
- [61] L. Rossi, A. Bobel, S. Wiedmann, R. Küchler, Y. Motome, K. Penc, N. Shannon, H. Ueda, and B. Bryant, Negative Thermal Expansion in the Plateau State of a Magnetically Frustrated Spinel, *Phys. Rev. Lett.* **123**, 027205 (2019).
- [62] L. Rossi, D. Brüning, H. Ueda, Y. Skourski, T. Lorenz, and B. Bryant, Magnetoelectric coupling in a frustrated spinel studied using high-field scanning probe microscopy, *Appl. Phys. Lett.* **116**, 262901 (2020).
- [63] J.-H. Chung, M. Matsuda, S.-H. Lee, K. Kakurai, H. Ueda, T. J. Sato, H. Takagi, K.-P. Hong, and S. Park, Statics and Dynamics of Incommensurate Spin Order in a Geometrically Frustrated Antiferromagnet  $\text{CdCr}_2\text{O}_4$ , *Phys. Rev. Lett.* **95**, 247204 (2005).
- [64] E. Kojima, A. Miyata, S. Miyabe, S. Takeyama, H. Ueda, and Y. Ueda, Full-magnetization of geometrically frustrated  $\text{CdCr}_2\text{O}_4$  determined by Faraday rotation measurements at magnetic fields up to 140 T, *Phys. Rev. B* **77**, 212408 (2008).
- [65] A. Miyata, H. Ueda, Y. Ueda, Y. Motome, N. Shannon, K. Penc, and S. Takeyama, Novel Magnetic Phases Revealed by Ultra-High Magnetic Field in the Frustrated Magnet  $\text{ZnCr}_2\text{O}_4$ , *J. Phys. Soc. Jpn.* **80**, 074709 (2011).
- [66] A. Miyata, H. Ueda, and S. Takeyama, Canted 2:1:1 Magnetic Supersolid Phase in a Frustrated Magnet  $\text{MgCr}_2\text{O}_4$  as a Small Limit of the Biquadratic Spin Interaction, *J. Phys. Soc. Jpn.* **83**, 063702 (2014).
- [67] M. Matsuda, H. Ueda, A. Kikkawa, Y. Tanaka, K. Katsumata, Y. Narumi, T. Inami, Y. Ueda, and S.-H. Lee, Spin-lattice instability to a fractional magnetization state in the spinel  $\text{HgCr}_2\text{O}_4$ , *Nat. Phys.* **3**, 397 (2007).
- [68] M. Matsuda, K. Ohoyama, S. Yoshii, H. Nojiri, P. Frings, F. Duc, B. Vignolle, G. L. J. A. Rikken, L.-P. Regnault, S.-H. Lee, H. Ueda, and Y. Ueda, Universal Magnetic Structure of the Half-Magnetization Phase in Cr-Based Spinel, *Phys. Rev. Lett.* **104**, 047201 (2010).
- [69] Y. Tanaka, Y. Narumi, N. Terada, K. Katsumata, H. Ueda, U. Staub, K. Kindo, T. Fukui, T. Yamamoto, R. Kammuri, M. Hagiwara, A. Kikkawa, Y. Ueda, H. Toyokawa, T. Ishikawa, and H. Kitamura, Lattice Deformations Induced by an Applied Magnetic Field in the Frustrated Antiferromagnet  $\text{HgCr}_2\text{O}_4$ , *J. Phys. Soc. Jpn.* **76**, 043708 (2007).
- [70] S. Kimura, S. Imajo, M. Gen, T. Momoi, M. Hagiwara, H. Ueda, and Y. Kohama, Quantum phase of the chromium spinel oxide  $\text{HgCr}_2\text{O}_4$  in high magnetic fields, *Phys. Rev. B* **105**, L180405 (2022).
- [71] N. V. Ter-Oganessian, Cation-ordered  $A'_{1/2}A''_{1/2}B_2X_4$  magnetic spinels as magnetoelectrics, *J. Magn. Magn. Mater.* **364**, 47 (2014).
- [72] A. Sundaresan and N. V. Ter-Oganessian, Magnetoelectric and multiferroic properties of spinels, *J. Appl. Phys.* **129**, 060901 (2021).
- [73] S. Gao, G. Pokharel, A. F. May, J. A. M. Paddison, C. Pasco, Y. Liu, K. M. Taddei, S. Calder, D. G. Mandrus, M. B. Stone, and A. D. Christianson, Line-graph approach to spiral spin liquids, *Phys. Rev. Lett.* **129**, 237202 (2022).